



# Deep Neural Network-Aided Histopathological Analysis of Myocardial Injury

Yiping Jiao<sup>1,2†</sup>, Jie Yuan<sup>1,2†</sup>, Oluwatofunmi Modupeoluwa Sodimu<sup>2</sup>, Yong Qiang<sup>1</sup> and Yichen Ding<sup>2,3\*</sup>

<sup>1</sup> Key Laboratory of Measurement and Control of CSE, Ministry of Education, School of Automation, Southeast University, Nanjing, China, <sup>2</sup> Department of Bioengineering, Erik Jonsson School of Engineering and Computer Science, The University of Texas at Dallas, Richardson, TX, United States, <sup>3</sup> Hamon Center for Regenerative Science and Medicine, The University of Texas Southwestern Medical Center, Dallas, TX, United States

## OPEN ACCESS

### Edited by:

Yun Fang,  
University of Chicago, United States

### Reviewed by:

Helen E. Collins,  
University of Louisville, United States  
Juhyun Lee,  
University of Texas at Arlington,  
United States

### \*Correspondence:

Yichen Ding  
yichen.ding@utdallas.edu

†These authors have contributed  
equally to this work

### Specialty section:

This article was submitted to  
Atherosclerosis and Vascular  
Medicine,  
a section of the journal  
Frontiers in Cardiovascular Medicine

Received: 12 June 2021

Accepted: 17 December 2021

Published: 10 January 2022

### Citation:

Jiao Y, Yuan J, Sodimu OM, Qiang Y  
and Ding Y (2022) Deep Neural  
Network-Aided Histopathological  
Analysis of Myocardial Injury.  
Front. Cardiovasc. Med. 8:724183.  
doi: 10.3389/fcvm.2021.724183

Deep neural networks have become the mainstream approach for analyzing and interpreting histology images. In this study, we established and validated an interpretable DNN model to assess endomyocardial biopsy (EMB) data of patients with myocardial injury. Deep learning models were used to extract features and classify EMB histopathological images of heart failure cases diagnosed with either ischemic cardiomyopathy or idiopathic dilated cardiomyopathy and non-failing cases (organ donors without a history of heart failure). We utilized the gradient-weighted class activation mapping (Grad-CAM) technique to emphasize injured regions, providing an entry point to assess the dominant morphology in the process of a comprehensive evaluation. To visualize clustered regions of interest (ROI), we utilized uniform manifold approximation and projection (UMAP) embedding for dimension reduction. We further implemented a multi-model ensemble mechanism to improve the quantitative metric (area under the receiver operating characteristic curve, AUC) to 0.985 and 0.992 on ROI-level and case-level, respectively, outperforming the achievement of  $0.971 \pm 0.017$  and  $0.981 \pm 0.020$  based on the sub-models. Collectively, this new methodology provides a robust and interpretive framework to explore local histopathological patterns, facilitating the automatic and high-throughput quantification of cardiac EMB analysis.

**Keywords:** deep neural network (DNN), heart failure, endomyocardial biopsy, histopathology (HPE), computer-aided diagnosis (CAD)

## INTRODUCTION

Heart failure is a major public health issue with a prevalence of over 23 million worldwide (1). Along with endomyocardial biopsy (EMB), non-invasive imaging methods such as an echocardiogram and magnetic resonance imaging (MRI) are the most common tools for diagnosing myocarditis, heart transplant rejection, and chemotherapy-induced injury (2, 3). EMB is a useful but invasive modality for making a definite diagnosis in diseases that are often difficult to diagnose by imaging modality alone. However, current grading methods in assessing histological patterns of myocardial injury are labor-intensive, error-prone, and suffer from a high inter-rater variability (4). Thus, a robust and reproducible method for the quantitative analysis of EMB is urgently needed.

Machine learning methods have been an integral part of biomedical research (5, 6) and clinical work (7, 8), having the great potential to overcome the intra- and inter-observer variability (9, 10)

and to improve diagnostic accuracy and efficiency (11). These computational models are based on algorithms that can extract features from clinical data (12). Compared to traditional machine learning methods that rely on expert knowledge to transform raw image data into features (e.g., texture, statistics, and wavelet transform coefficients) (13, 14), deep neural networks (DNN) can achieve better accuracy without defining features explicitly. In the field of cardiovascular diseases, deep learning has been widely implemented for image classification and segmentation in multiple modalities, including echocardiography, coronary artery calcium scoring, coronary computed tomography angiography, single-photon emission computed tomography, positron emission tomography, magnetic resonance imaging, and optical coherence tomography (8, 15–17).

Histopathological image analysis remains the gold standard for diagnosing many diseases. DNN has been proven to be a powerful approach in the analysis of histopathological images of tumor specimens; DNN can predict tumor metastasis (11) and has been shown to be useful for tumor grading (18) and tumor microenvironment analysis (19). While some researchers reported the implementation of DNN into EMB images, the interpretability of DNN output remains challenging.

This study established and validated an interpretable DNN model to assess EMB data of patients with myocardial injury. To extract and classify representative features of myocardial injury on local histological patterns, we adapted a well-established VGG-19 model (20). We then applied the other two methods, gradient-weighted class activation mapping (Grad-CAM) (21) and uniform manifold approximation and projection (UMAP) embedding method (22), to elucidate the model outputs and visualize the intermediate features made by the VGG-19 model. Moreover, we introduced a novel multi-model ensemble strategy to minimize the intra- and inter-observer variability of random dataset partition. Collectively, our method enables automatic quantification of EMB images related to cardiomyopathy, creating a series of visualizable archives for efficient and accurate pathological inspection and providing new insight into cardiac image analysis enhanced by machine learning.

## MATERIALS AND METHODS

### Data Collection

We used a publicly available dataset provided in a previous study for DNN model development and evaluation (23). Hematoxylin and eosin (H&E) stained EMB tissue samples were collected from left ventricles of 209 patients registered at the University of Pennsylvania, including 94 end-stage heart failure cases diagnosed with either ischemic cardiomyopathy ( $n = 51$ ) or idiopathic dilated cardiomyopathy ( $n = 43$ ), and 115 non-failure cases (23). The non-failure cases were organ donors without a history of heart failure; the hearts were not used for transplantation. Each case included 11 random ROIs within the myocardium, corresponding to 11 specific areas of  $50 \times 50 \mu\text{m}^2$ , i.e.,  $250 \times 250$  pixels.

In machine learning, a dataset is usually divided as a training set, validation set, and held-out test set, used for model training,

**TABLE 1** | Number of cases used in the model development and validation.

Subset partition		Non-failure	Failure
Individual model (Development set)	Training	38	32
	Validation	19	15
Multi-model ensemble (Development set)	Fold-1	12	10
	Fold-2	12	10
	Fold-3	11	9
	Fold-4	11	9
	Fold-5	11	9
Held-out test set		58	47

*Each case includes 11 regions of interest (ROIs).*

model tuning, and evaluation, respectively. In this study, the aforementioned dataset was divided on case-level into the development set (104 cases, corresponding to 1144 ROIs) for training and validation or multi-model ensemble, and the held-out test set (105 cases, corresponding to 1155 ROIs), removing the crosstalk between development and test sets.

A single model was trained on the well-established development set (23), including 70 cases (770 ROIs) for training and 34 cases (374 ROIs) for validation (Table 1). We further employed a multi-model ensemble mechanism using the five-fold-based cross-validation (see **Cross-validation for multi-model ensemble**), where 10 models were trained and integrated to improve accuracy.

### Deep Neural Network for Myocardium Assessment

We used VGG-19 network (20) to analyze EMB images. VGG-19 network has been widely used in computational pathology (24, 25). The first part of the model was composed of 16 convolutional layers and five max-pooling layers as the feature extractor. The rest of the model was composed of a global average pooling (GAP) layer and a classification layer with two nodes (Figure 1A). In comparison to the original VGG-19 network, our model is light-weighted and compatible with other parts of our framework (see **Regional and feature interpretability**). In our classification task, an input image was processed by all the layers and turned into a probability distribution ( $p_F$  or  $p_N$ ) among all the classes in the output layer (Figure 1A). From an overall view, the model receives input image of shape  $224$  (width)  $\times$   $224$  (height)  $\times$   $3$  (channels), and outputs a Bernoulli distribution, where the  $p_F$  activation gives the possibility that the input image is acquired from a heart failure patient. The entire model can be automatically optimized by minimizing the discrepancy between the network activation and desired output for end-to-end training.

### Regional and Feature Interpretability

We employed the Grad-CAM method (21) to highlight the potentially injured regions projected for interpretation and implemented the UMAP embedding to visualize inter-sample similarity generated by our VGG-19 model.

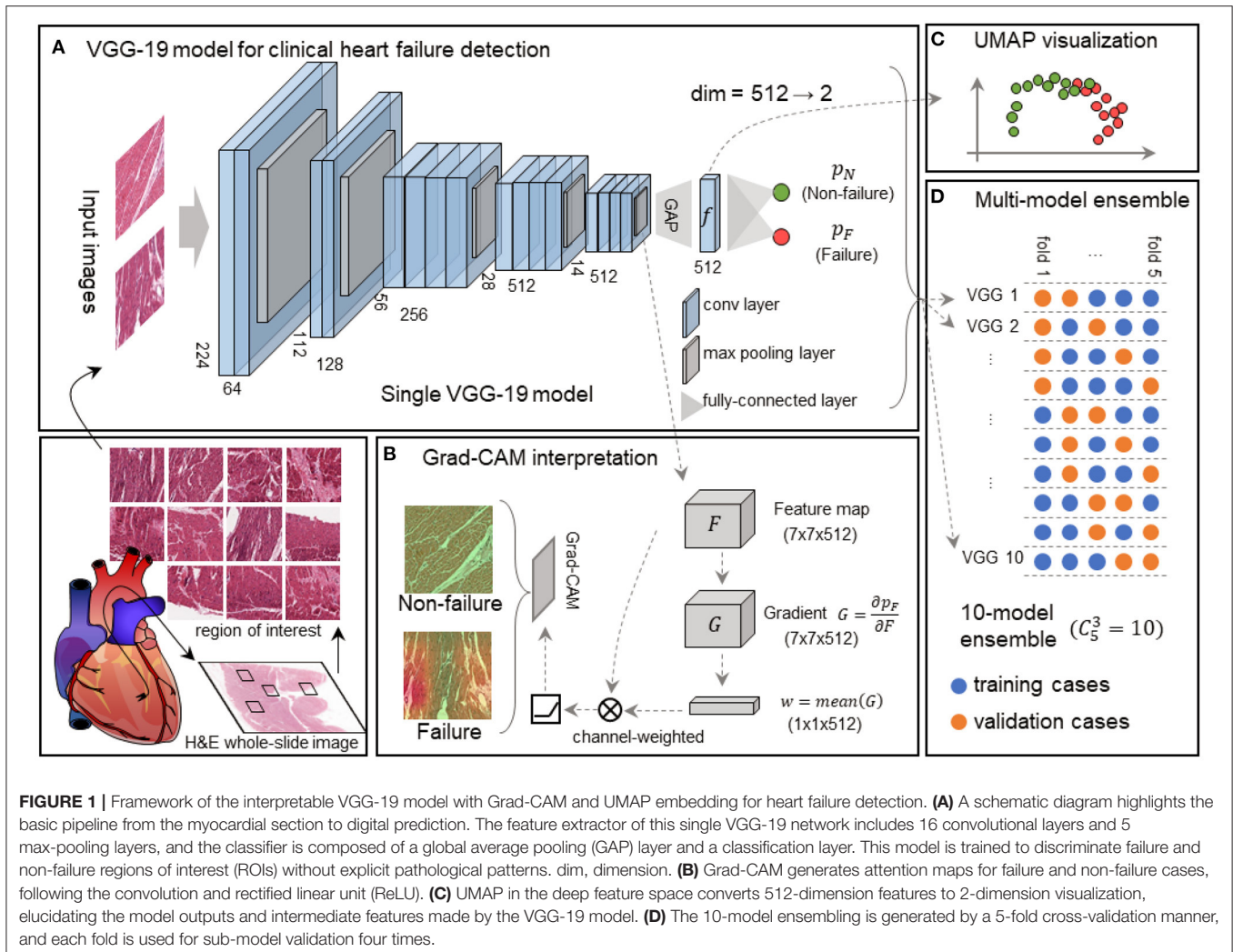


**FIGURE 1** | Framework of the interpretable VGG-19 model with Grad-CAM and UMAP embedding for heart failure detection. **(A)** A schematic diagram highlights the basic pipeline from the myocardial section to digital prediction. The feature extractor of this single VGG-19 network includes 16 convolutional layers and 5 max-pooling layers, and the classifier is composed of a global average pooling (GAP) layer and a classification layer. This model is trained to discriminate failure and non-failure regions of interest (ROIs) without explicit pathological patterns. dim, dimension. **(B)** Grad-CAM generates attention maps for failure and non-failure cases, following the convolution and rectified linear unit (ReLU). **(C)** UMAP in the deep feature space converts 512-dimension features to 2-dimension visualization, elucidating the model outputs and intermediate features made by the VGG-19 model. **(D)** The 10-model ensembling is generated by a 5-fold cross-validation manner, and each fold is used for sub-model validation four times.

The  $7 \times 7 \times 512$  tensor was obtained from the feature extractor conveys abstract semantic information to the Grad-CAM to generate an attention map (Figure 1B) and UMAP to reduce the dimension (Figure 1C). We defined the output tensor from the last pooling layer in the VGG-19 model as  $F$ , and the predicted failure probability as  $p_F$ . Grad-CAM calculated the gradient as  $G = \frac{\partial p_F}{\partial F}$ , followed by a global-average pooling as a convolutional kernel  $w$ . Given an input size of  $224 \times 224 \times 3$ , the output size of  $F$ ,  $G$ , and  $w$  were  $7 \times 7 \times 512$ ,  $7 \times 7 \times 512$ , and  $1 \times 1 \times 512$ , respectively. The final attention map ( $A$ ) is determined as follows:

$$A = \text{ReLU}(F \otimes w),$$

where  $\otimes$  represents convolutional operation, and ReLU is defined as:

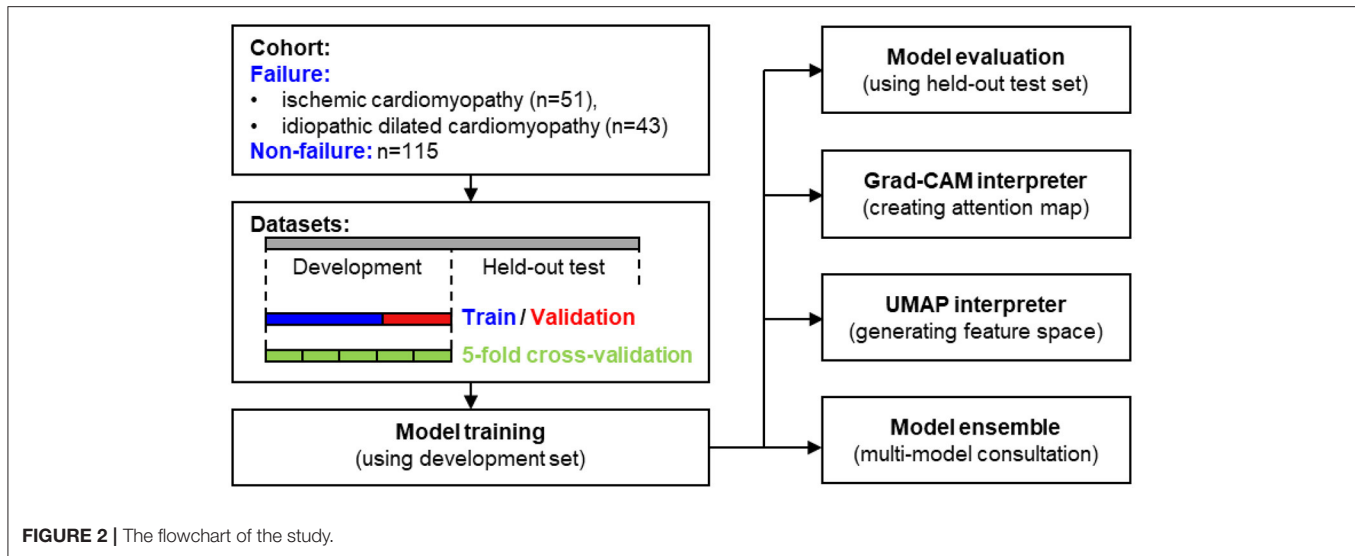
$$\text{ReLU}(x) = x \text{ if } x > 0 \text{ else } 0.$$

The attention map highlights the regions in an input image that are mostly responsible for prediction. Thus, it provides a way to interpret the decision made by the deep neural network.

In addition to the region-based interpretation, we utilized the UMAP embedding technique to reveal the discrepancy between failing samples and non-failing samples in the feature space. We gathered deep features immediately before the final classification layer. Each input image corresponds to a deep feature vector with a length of 512. Next, we calculated the pair-wise Euclidean distances among all the ROIs, and the distance matrix was processed by UMAP (22), resulting in a 2-D embedding for each ROI. The embedding could be visualized as a scatter plot (Figure 1C), reflecting the spatial relationships among samples.

### Cross-Validation for Multi-Model Ensemble

Cross-validation is widely used to evaluate the performance of machine learning models reliably in small datasets. The dataset is generally partitioned to  $K$  portions, where each portion is known as a “fold.” Based on the partition, we usually use arbitrary  $m = K - 1$  portions to train a model and evaluate



its performance on the rest of one portion. For this reason, we further introduced this multi-model ensemble mechanism based on cross-validation to mimic multiple human experts for consultation in pathology and minimize the randomness caused by dataset partition. We partitioned the development set into  $K = 5$  subsets on case-level (Table 1) and used  $m = 3$  out of  $K = 5$  subsets to train a sub-model and the rest for validation at each time. All the  $C_K^m = 10$  models were independently trained with the identical protocol above. This allowed us to generate  $C_{K-1}^{K-m-1} = 4$  independent predictions to validate the training process prior to the model deployment on the held-out test set (Figure 1D). The final decision from the multi-model ensemble relied on the averaging results to eliminate the discrepancy among individual models. The whole strategy of the multi-model ensemble mechanism is similar to the pathology consultation in which experience and knowledge vary from different experts, providing a comprehensive insight into ambiguous cases.

## EXPERIMENTS AND RESULTS

The study flowchart is shown in Figure 2. Given the study cohort, image samples, and partitioned datasets, both individual model and multi-model ensemble were trained and evaluated for clinical heart failure detection. Furthermore, we integrated model interpretation techniques, including Grad-CAM-based regional visualization and UMAP-based feature space visualization, to generate positive predictions for specific local histological patterns such as fibrous infiltration and the enlarged myocardial cell nuclei.

### Training and Validation of an Individual Model

We established an individual VGG-19 model on 770 training ROIs from 38 non-failure and 32 failure cases. The model was validated using 19 non-failure and 15 failure cases in 100 epochs (Table 1). The model was initialized with parameters pre-trained

on ImageNet (20). The trainable parameters were then optimized by an Adam optimizer (26) (with a constant learning rate of  $10^{-4}$ ) to minimize cross-entropy loss:

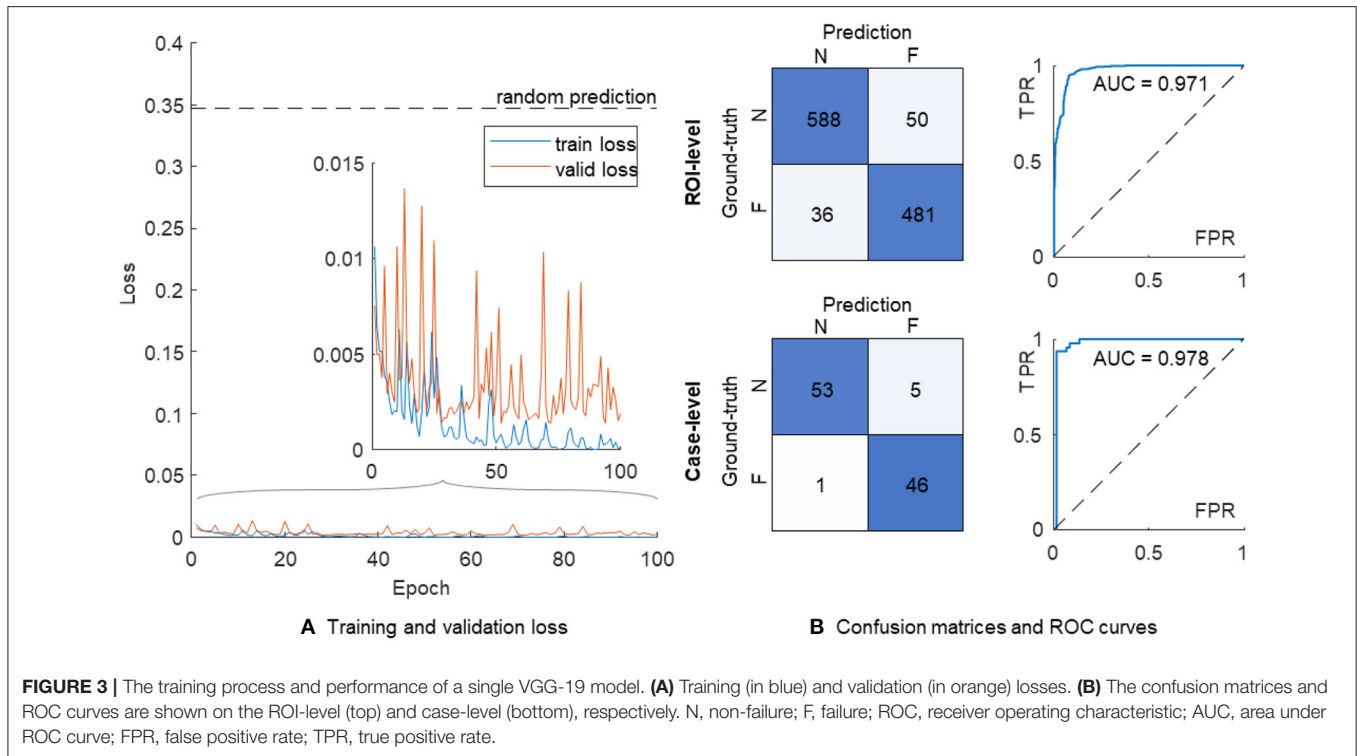
$$L = \frac{1}{|C|} \sum_{c \in C} -y_c \log(\hat{y}_c),$$

where  $C$  is the label set of the dataset,  $y_c \in \{0, 1\}$  is the one-hot encoded label of a sample, and  $\hat{y}_c$  is the corresponding prediction obtained from the output layer of the network. In response to appearance variation among numerous ROIs, we adopted data augmentation techniques, including random 224-pixel cropping, horizontal and vertical flipping, and stain augmentation (27) in the training process. Both training and validation losses were calculated and recorded at the end of each training period. The optimal network parameters with the lowest validation loss were retrieved for the assessment on the held-out test set (Figure 3A).

The confusion matrix on the ROI level showed 588 and 481 correct classifications in 638 non-failure and 517 failure cases, respectively (Figure 3B). We further used the proportion of positive predictions of heart failure among 11 ROIs in each patient as the aggregated risk score on the case level, achieving 53 and 46 correct classifications out of 58 non-failure and 47 failure cases, respectively. The AUC values were 0.971 and 0.978 on the ROI- and case-level, respectively.

### Grad-CAM-Based Local Visualization

We implemented the Grad-CAM to map the positive confidence to corresponding locations in the raw EMB images, demonstrating that the predictive capability of the VGG-19 model is correlated with dominant morphology such as enlarged nuclei (Figures 4A,B), inflammatory infiltration (Figure 4C), and perinuclear vacuolation (Figure 4D). All the morphologies above were labeled as high attention (arrows in the top panel and corresponding regions in the bottom) in contrast to the medium or low attention in surroundings. The results implied that this deep model could recognize specific



morphological patterns in the local area on the ROI. The Grad-CAM provided a straightforward visualization method to interpret the complicated features from the DNN model, guiding us to concentrate on delicate inspection in high attention regions. We further highlighted that Grad-CAM automatically generated attention maps in accordance with pathologies, indicating that this model learned a certain level of pathological knowledge bypassing explicitly defined pathological patterns. Collectively, the attention map visualization improved the credibility and interpretability of the deep models.

### UMAP Embedding-Based Global Feature Space Visualization

The UMAP embedding method reduced the dimensionality of the intermediate tensor at the end of the feature extractor in the VGG-19 model, following a GAP layer. We converted all images in the development set and the held-out test set to 512 × 1 column vectors and used the UMAP method to generate 2-D embeddings of all the images. The failure and non-failure samples were mixed together and could not be divided if processed by dimension reduction in the feature space of the original VGG-19 model (Figure 5A). In comparison, our retrained model generated a clear boundary between two groups showing regular distribution in the deep feature space (Figure 5B). This suggests that the feature extractor is effectively re-modulated in the heart failure detection task.

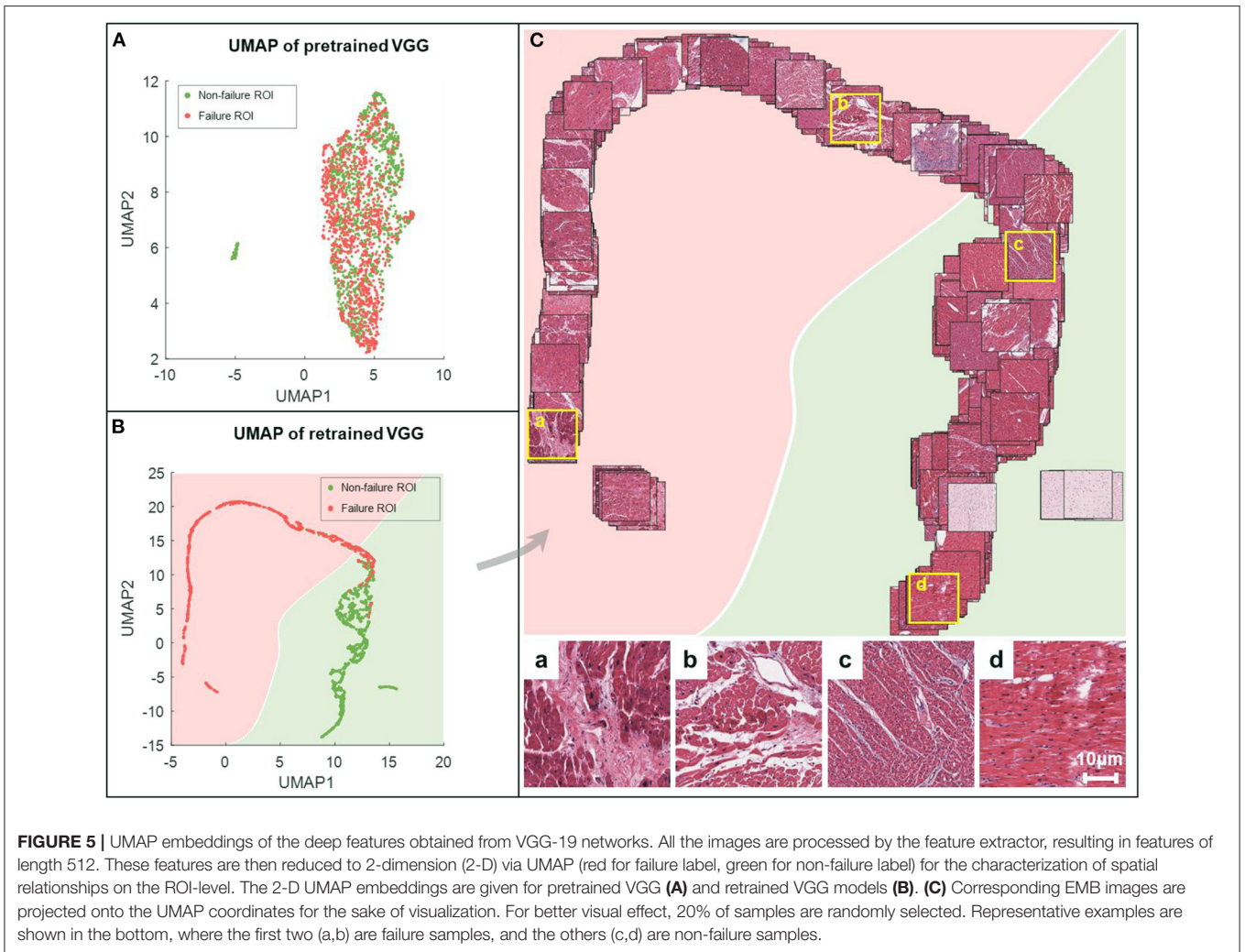
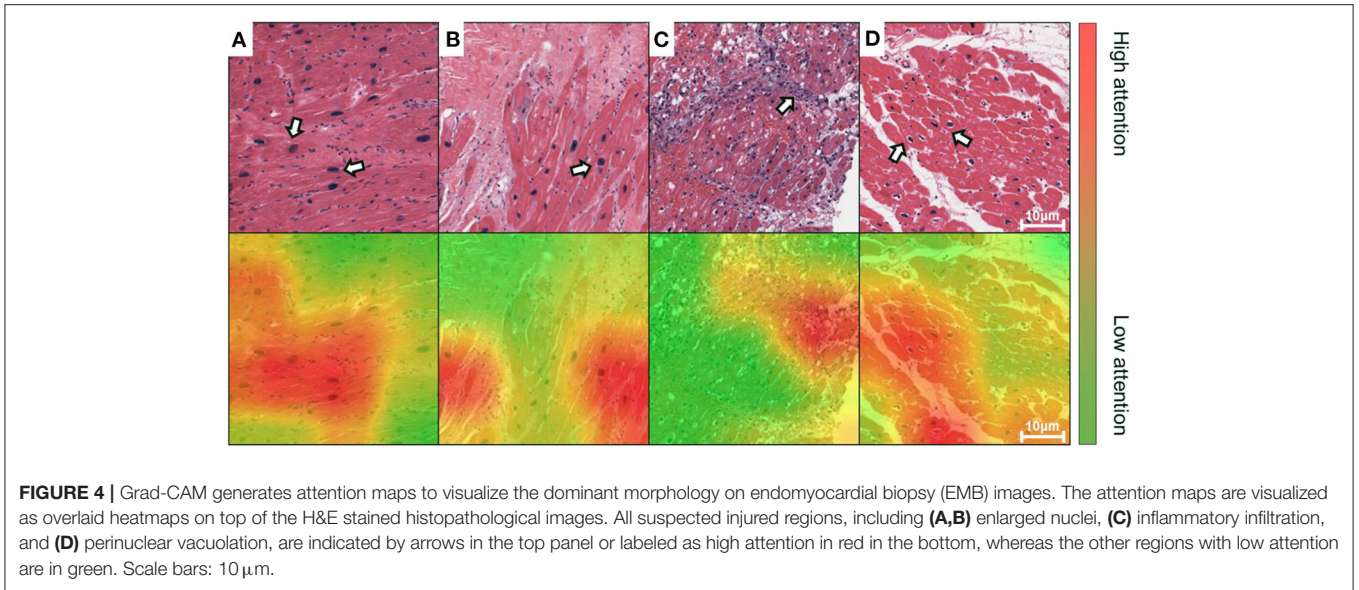
We further projected all ROIs to the corresponding coordinates in the UMAP space, providing an intuitive distribution of non-failure (in green) and failure (in pink) images (Figure 5C). Compared to the failure group, the non-failure

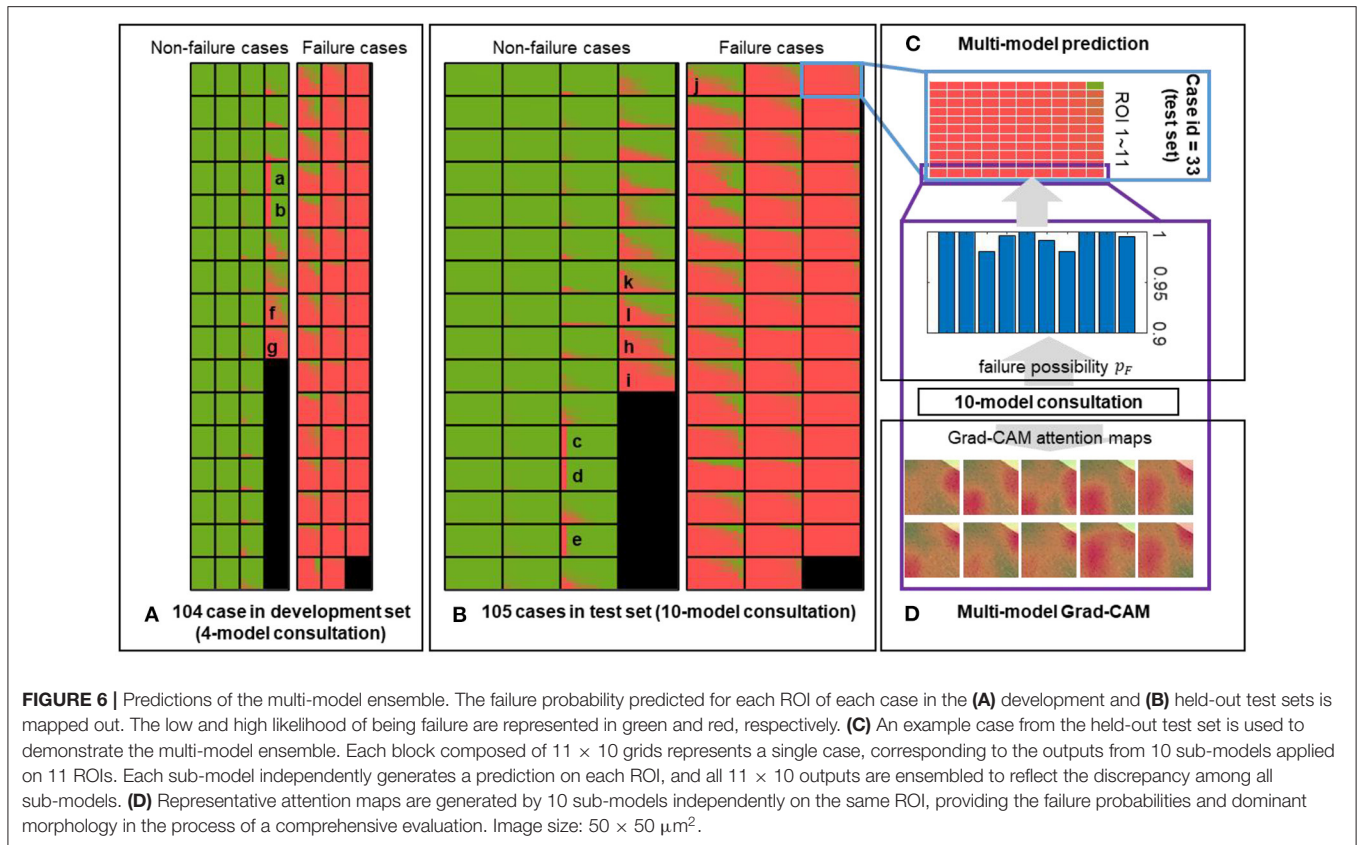
images were correlated with densely arranged myocardium cells. Our results indicated that the VGG-19 model was still sensitive to specific applications, and retraining was mandatory to improve the generalization capability.

### Multi-Model Ensemble

In addition to the individual model, we employed the multi-model ensemble to mimic multiple human experts for consultation, and each sub-model served as an expert with different background. This method allowed us to verify the predictions made by different models trained on different datasets (Table 1). We divided 104 cases in the development set into five portions to generate 10 independent sub-models, and each portion was used for validation (in orange) four times in the development (Figure 1D). Thus, each case included 11 × 4 grids in Figure 6A. We further implemented these 10 sub-models into the held-out test set (Figure 6B), generating 11 × 10 grids for each case to assess the injured regions on 11 ROIs (Figure 6C). We mapped out the integrative reports of all 209 cases in Figure 6, accentuating the individual prediction of each ROI in each case from all available models. In both development and test sets, most non-failure cases had low failure risk predictions (in green) and vice versa (in red). Besides the predicted likelihood of being a failure, our model could simultaneously generate multiple attention maps, providing more intuitive evidence for further predictive decisions on ambiguous cases (Figure 6D).

We averaged corresponding likelihood scores to quantify the prediction on the ROI- and case-level. In comparison with the results of the individual model (Figure 3B), the multi-model ensemble performed 604 and 483 correct classifications on the





ROI-level, and detected 56 true non-failure and 46 true failure cases on the case-level (Figure 7). The AUC values of the ensemble model were 0.985 and 0.992 on the ROI- and case-level, respectively, exceeding the average of the 10 sub-models [AUC =  $0.971 \pm 0.017$  and  $0.981 \pm 0.020$  (mean  $\pm$  standard deviation), respectively], and the AUC values achieved by random forest (AUC = 0.933 and 0.952), and two pathologists (AUC = 0.75, 0.73, on case-level) (23). The quantitative results demonstrated that our multi-model ensemble reduced the misclassification rate, especially on the non-failure cases, and improved the AUC values on both ROI- and case-levels, suggesting its ability to serve as a great complimentary tool to assist clinical diagnosis.

## DISCUSSIONS

While the clinical diagnosis of heart failure relies on ejection fraction and serum biomarker, EMB is always a useful method for making a definite diagnosis in diseases that are difficult to diagnose by imaging modality alone. Computational pathology techniques based on the deep learning method can reduce the workload on pathologists, particularly for regions that have shortages in access to pathological diagnosis services. Nevertheless, the interpretability issue affects people's trust in deep learning systems. This study established and validated an interpretable DNN model to assess EMB histopathology in response to myocardial injury.

We demonstrated that the well-trained VGG-19 network could distinguish heart failure cases from the non-failure ones using local ROIs selected on whole-slide images. Different from traditional methods that rely on explicit pathological patterns such as cell types (28) or morphological features (29), our model was trained with failure or non-failure label solely. However, the attention maps generated by Grad-CAM were well-localized with representative morphologies such as enlarged nuclei and irregular shapes of cells, indicating that the extracted features from our model pertain to a certain level of pathological knowledge. Combined with Grad-CAM and UMAP embedding methods, we further provided an intuitive visualization of the local and global feature patterns of all EMB images learned by the VGG-19 model. Unlike other applications in cancer (24, 30–32), the implementation of this new model in myocardial injury reveals ill-defined histopathological patterns in local regions, providing a guideline and attention maps for well-trained pathologists. Therefore, integrating VGG-19 with Grad-CAM and UMAP embedding methods provides an interpretive DNN model for more accurate histopathological analyses.

Our method can be used to obtain the predictive results of each ROI from all ensembled sub-models, leading to an intuitive illustration of the discrepancy among individual sub-models (Figure 8, corresponding to representative results in Figure 6). In this study, we emphasized two types of disagreements among sub-models: (1) a significantly different prediction generated by a sub-model (Figures 8A–E, corresponding to A–E in Figure 6),

and (2) in distinguishing false positive or false negative results (Figures 8F–J, corresponding to F–J in Figure 6). The former disagreement is due to the varied staining appearance of specific cases (Figures 8A–E), resulting in an incomprehensive training dataset. Specifically, the data distribution should be inspected prior to model development in response to negative effects introduced by the domain shift (33). The cross-validation protocol employed in this study provides a way to observe such

effects in the training dataset. The latter type of disagreement (Figures 8F–J) pertains to transitional predictions, an ambiguous case-related false-positive or false-negative result. In some cases, with the label of “non-failure” (e.g., Figures 8K,L, corresponding to K and L in Figure 6), a few ROIs receive high-risk scores. While the case-level predictions match the ground truth, such circumstance indicates that the case may exhibit severe local injury. To address this issue, we will gather more representative samples, investigate the whole-slide image instead of some specific ROIs, and incorporate other supplementary approaches such as immunohistochemistry staining and polymerase chain reaction (PCR)-based analysis for a comprehensive assessment.

DNN has been proved as a generalizable tool in assisting cardiovascular disease diagnosis, for example, evaluating cardiac allograft rejection by analyzing histopathological or multiplex immunofluorescence images (4, 34). DNN has also led to breakthroughs in other imaging modalities for cardiovascular diagnosis or research, such as echocardiography, coronary artery calcium scoring, coronary computed tomography angiography, light-sheet microscopy, light-field imaging, etc. (17, 35, 36). Numerous applications such as quantification of receptor status (37), estimation of Ki-67 index (38), or implementation into Ziehl-Neelsen staining (39) and Masson’s Trichrome (40) are potentially feasible in cardiovascular studies as well. Besides generic image classification and segmentation, DNN has demonstrated its viability to synthesize pseudo H&E images from Raman spectroscopy and other multi-modality non-linear imaging techniques, augmenting non-invasive and *in vivo* diagnosis (41). Collectively, the proposed framework provides a general pipeline for most of modalities and applications, improving the reliability and credibility of deep learning methods in cardiovascular diagnosis and research.

As a data-driven model, an unbiased and comprehensive training dataset is always preferred in an ideal condition. Our current model can be improved from the following aspects. First, the model was trained supervisory with a case-level label (belonging to failure or non-failure group). While

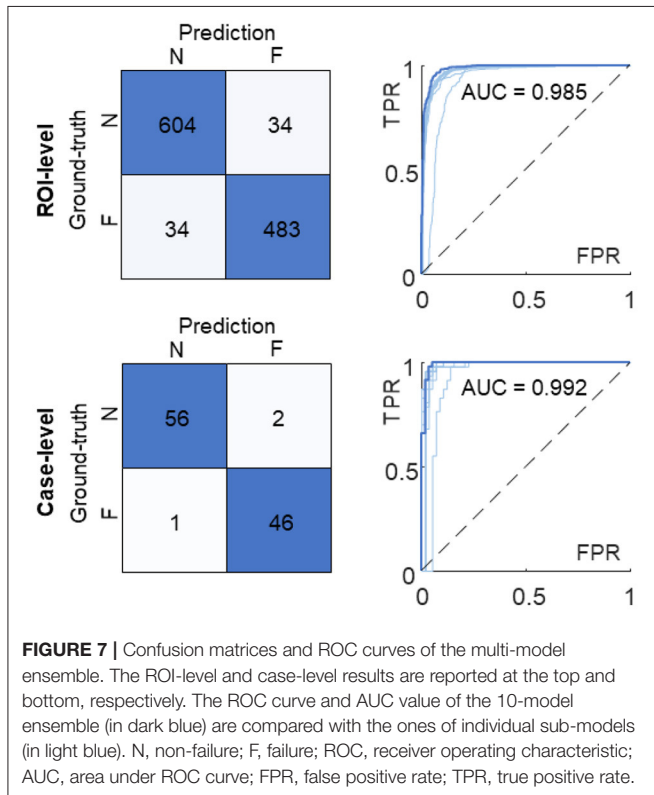


**FIGURE 7 |** Confusion matrices and ROC curves of the multi-model ensemble. The ROI-level and case-level results are reported at the top and bottom, respectively. The ROC curve and AUC value of the 10-model ensemble (in dark blue) are compared with the ones of individual sub-models (in light blue). N, non-failure; F, failure; ROC, receiver operating characteristic; AUC, area under ROC curve; FPR, false positive rate; TPR, true positive rate.

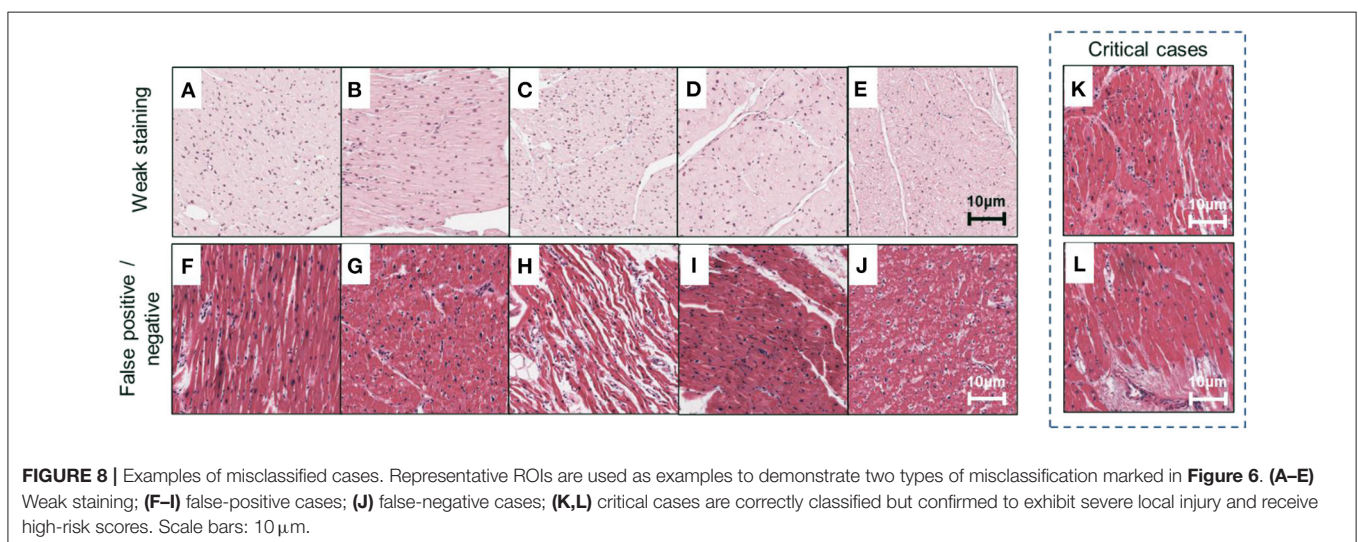


**FIGURE 8 |** Examples of misclassified cases. Representative ROIs are used as examples to demonstrate two types of misclassification marked in Figure 6. (A–E) Weak staining; (F–I) false-positive cases; (J) false-negative cases; (K,L) critical cases are correctly classified but confirmed to exhibit severe local injury and receive high-risk scores. Scale bars: 10  $\mu$ m.



the high attention regions are correlated with pathological patterns, these patterns are not explicitly defined and cannot be quantified by DNNs. We will further introduce additional labels to characterize specific pathological patterns, for example, infiltrated inflammation and myocardial necrosis (12). Second, our data were provided by a single institute. We plan to include more diverse data sources to address the issues of varying data quality, processing protocol, and the equipment used for sample preparation (42). A more robust model covering the sample diversity may further advance future clinical investigations.

## CONCLUSION

In this study, we integrated the VGG-19 network with Grad-CAM, UMAP, and multi-model ensemble methods for assessing EMB images from heart failure cases, providing an interpretive classification with high efficiency and accuracy. Three strategies, including the attention maps produced by Grad-CAM, the deep feature visualization via UMAP embedding, and multi-model ensemble, facilitated the interpretability of this VGG-19 model and clarified the dominant morphologies of injured regions on EMB images. Both individual model and multi-model ensemble indicated that DNN-aided diagnosis had great potential to recognize cardiomyopathy. Overall, our method established the basis for quantitative computation and intuitive interpretation of EMB images that can advance the applications of deep learning models in cardiac research.

## REFERENCES

- Bui AL, Horwich TB, Fonarow GC. Epidemiology and risk profile of heart failure. *Nat Rev Cardiol.* (2011) 8:30–41. doi: 10.1038/nrcardio.2010.165
- Veinot JP. Endomyocardial biopsy—when, and how? *Cardiovasc Pathol.* (2011) 20:291–6. doi: 10.1016/j.carpath.2010.08.005
- Pollack A, Kontorovich AR, Fuster V, Dec GW. Viral myocarditis—diagnosis, treatment options, current controversies. *Nat Rev Cardiol.* (2015) 12:670–80. doi: 10.1038/nrcardio.2015.108
- Peyster EG, Arabyarmohammadi S, Janowczyk A, Azarianpour-Esfahani S, Sekulic M, Cassol C, et al. An automated computational image analysis pipeline for histological grading of cardiac allograft rejection. *Eur Heart J.* (2021) 42:2356–69. doi: 10.1093/eurheartj/ehab241
- Orringer DA, Pandian B, Niknafs YS, Hollon TC, Boyle J, Lewis S, et al. Rapid intraoperative histology of unprocessed surgical specimens via fibre-laser-based stimulated raman scattering microscopy. *Nat Biomed Eng.* (2017) 1:0027. doi: 10.1038/s41551-016-0027
- Savastano LE, Zhou Q, Smith A, Vega K, Murga-Zamalloa C, Gordon D, et al. Multimodal laser-based angioscopy for structural, chemical and biological imaging of atherosclerosis. *Nat Biomed Eng.* (2017) 1:0023. doi: 10.1038/s41551-016-0023
- Esteva A, Kuprel B, Novoa RA, Ko J, Swetter SM, Blau HM, et al. Dermatologist-level classification of skin cancer with deep neural networks. *Nature.* (2017) 542:115–8. doi: 10.1038/nature21056
- Hannun AY, Rajpurkar P, Haghpanahi M, Tison GH, Bourn C, Turakhia MP, et al. Cardiologist-level arrhythmia detection and classification in ambulatory electrocardiograms using a deep neural network. *Nat Med.* (2019) 25:65–9. doi: 10.1038/s41591-018-0268-3
- Loh BCS, Then PHH. Deep learning for cardiac computer-aided diagnosis: benefits, issues & solutions. *mHealth.* (2017) 3:45. doi: 10.21037/mhealth.2017.09.01

## DATA AVAILABILITY STATEMENT

Publicly available datasets were analyzed in this study. This data can be found at: The image data supporting this study can be found via <https://idr.openmicroscopy.org/webclient/?show=project-402>.

## AUTHOR CONTRIBUTIONS

YJ, JY, and YD contributed to the development of the intellectual design of the project. YJ and JY performed the experiments and prepared the manuscript. All authors contributed to the data analysis, manuscript revision, and final approval.

## FUNDING

This work was supported by NIH R00 HL148493 (YD), NSFC 62103098 (JY), and the University of Texas at Dallas.

## ACKNOWLEDGMENTS

The authors would like to thank Dr. Anant Madabhushi for sharing the dataset that supports this study. We also thank YW for his help with interpretation of the Grad-CAM attention maps.

- Jahmunah V, Oh SL, Wei JKE, Ciaccio EJ, Chua K, San TR, et al. Computer-aided diagnosis of congestive heart failure using ECG signals – a review. *Physica Medica.* (2019) 62:95–104. doi: 10.1016/j.ejmp.2019.05.004
- Bejnordi BE, Veta M, Van Diest PJ, Van Ginneken B, Karssemeijer N, Litjens G, et al. Diagnostic assessment of deep learning algorithms for detection of lymph node metastases in women with breast cancer. *JAMA.* (2017) 318:2199–210. doi: 10.1001/jama.2017.14585
- Peyster EG, Madabhushi A, Margulies KB. Advanced morphologic analysis for diagnosing allograft rejection: the case of cardiac transplant rejection. *Transplantation.* (2018) 102:1230–9. doi: 10.1097/TP.0000000000002189
- Faust O, Acharya UR, Sudarshan VK, Tan RS, Yeong CH, Molinari F, et al. Computer aided diagnosis of coronary artery disease, myocardial infarction and carotid atherosclerosis using ultrasound images: a review. *Physica Medica.* (2017) 33:1–15. doi: 10.1016/j.ejmp.2016.12.005
- Ding Y, Gudapati V, Lin R, Fei Y, Packard RRS, Song S, et al. Saak transform-based machine learning for light-sheet imaging of cardiac trabeculation. *IEEE Trans Biomed Eng.* (2021) 68:225–35. doi: 10.1109/TBME.2020.2991754
- Kang SH, Joe B, Yoon Y, Cho GY, Shin I, Suh JW. Cardiac auscultation using smartphones: pilot study. *JMIR Mhealth Uhealth.* (2018) 6:e49. doi: 10.2196/mhealth.8946
- Hill NR, Ayoubkhani D, McEwan P, Sugrue DM, Farooqui U, Lister S, et al. Predicting atrial fibrillation in primary care using machine learning. *PLoS ONE.* (2019) 14:e0224582. doi: 10.1371/journal.pone.0224582
- Al'Aref SJ, Anchouche K, Singh G, Slomka PJ, Kolli KK, Kumar A, et al. Clinical applications of machine learning in cardiovascular disease and its relevance to cardiac imaging. *Eur Heart J.* (2019) 40:1975–86. doi: 10.1093/eurheartj/ehy404
- Tolkach Y, Dohmgörgen T, Toma M, Kristiansen G. High-accuracy prostate cancer pathology using deep learning. *Nat Mach Intell.* (2020) 2:411–8. doi: 10.1038/s42256-020-0200-7
- Jiao Y, Li J, Qian C, Fei S. Deep learning-based tumor microenvironment analysis in colon adenocarcinoma histopathological

- whole-slide images. *Comput Methods Programs Biomed.* (2021) 204:106047. doi: 10.1016/j.cmpb.2021.106047
20. Simonyan K, Zisserman A. Very deep convolutional networks for large-scale image recognition. *arXiv [Preprint]*. arXiv:1409.1556 (2014).
  21. Selvaraju RR, Cogswell M, Das A, Vedantam R, Parikh D, Batra, et al. *Grad-CAM: Visual Explanations from Deep Networks via Gradient-Based Localization*. IEEE International Conference on Computer Vision (ICCV). Venice; IEEE (2017). p. 618–26.
  22. McInnes L, Healy J, Melville J. Umap: Uniform manifold approximation and projection for dimension reduction. *arXiv [Preprint]*. arXiv:1802.03426 (2018).
  23. Nirschl JJ, Janowczyk A, Peyster EG, Frank R, Margulies KB, Feldman MD, et al. A deep-learning classifier identifies patients with clinical heart failure using whole-slide images of h&e tissue. *PLoS ONE.* (2018) 13:e0192726. doi: 10.1371/journal.pone.0192726
  24. Faust K, Bala S, van Ommeren R, Portante A, Al Qawahmed R, Djuric U, et al. Intelligent feature engineering and ontological mapping of brain tumour histomorphologies by deep learning. *Nat Mach Intell.* (2019) 1:316–21. doi: 10.1038/s42256-019-0068-6
  25. Kather JN, Pearson AT, Halama N, Jäger D, Krause J, Loosen SH, et al. Deep learning can predict microsatellite instability directly from histology in gastrointestinal cancer. *Nat Med.* (2019) 25:1054–6. doi: 10.1038/s41591-019-0462-y
  26. Kingma DP, Ba J. Adam: A method for stochastic optimization. *arXiv [Preprint]*. arXiv:1412.6980 (2014).
  27. Tellez D, Litjens G, Bándi P, Bulten W, Bokhorst JM, Ciompi F, et al. Quantifying the effects of data augmentation and stain color normalization in convolutional neural networks for computational pathology. *Med Image Anal.* (2019) 58:101544. doi: 10.1016/j.media.2019.101544
  28. Diao JA, Wang JK, Chui WF, Mountain V, Gullapally SC, Srinivasan R, et al. Human-interpretable image features derived from densely mapped cancer pathology slides predict diverse molecular phenotypes. *Nat Comm.* (2021) 12:1613. doi: 10.1038/s41467-021-21896-9
  29. Phillip JM, Han KS, Chen WC, Wirtz D, Wu PH. A robust unsupervised machine-learning method to quantify the morphological heterogeneity of cells and nuclei. *NatProtoc.* (2021) 16:754–74. doi: 10.1038/s41596-020-00432-x
  30. Faust K, Xie Q, Han D, Goyle K, Volynskaya Z, Djuric U, et al. Visualizing histopathologic deep learning classification and anomaly detection using nonlinear feature space dimensionality reduction. *BMC Bioinform.* (2018) 19:173. doi: 10.1186/s12859-018-2184-4
  31. Silva-Rodríguez J, Colomer A, Sales MA, Molina R, Naranjo V. Going deeper through the gleason scoring scale: an automatic end-to-end system for histology prostate grading and cribriform pattern detection. *Comput Methods Programs Biomed.* (2020) 195:105637. doi: 10.1016/j.cmpb.2020.105637
  32. Jiang S, Li H, Jin Z. A visually interpretable deep learning framework for histopathological image-based skin cancer diagnosis. *IEEE J Biomed Health Inform.* (2021) 25:1483–94. doi: 10.2307/j.ctv1gt945c.26
  33. Stacke K, Eilertsen G, Unger J, Lundström C. A closer look at domain shift for deep learning in histopathology. *arXiv [Preprint]*. arXiv:1909.11575 (2019).
  34. Peyster EG, Wang C, Ishola F, Remeniuk B, Hoyt C, Feldman MD, et al. In situ immune profiling of heart transplant biopsies improves diagnostic accuracy and rejection risk stratification. *JACC Basic Transl Sci.* (2020) 5:328–40. doi: 10.1016/j.jacbts.2020.01.015
  35. Wang Z, Zhu L, Zhang H, Li G, Yi C, Li Y, et al. Real-time volumetric reconstruction of biological dynamics with light-field microscopy and deep learning. *Nat Methods.* (2021) 18:551–6. doi: 10.1038/s41592-021-01058-x
  36. Wang Z, Ding Y, Satta S, Roustaei M, Fei P, Hsiai, et al. A hybrid of light-field and light-sheet imaging to study myocardial function and intracardiac blood flow during zebrafish development. *PLoS Comput Biol.* (2021) 17:e1009175. doi: 10.1371/journal.pcbi.1009175
  37. Saha M, Arun I, Ahmed R, Chatterjee S, Chakraborty C. Hscorenet: a deep network for estrogen and progesterone scoring using breast IHC images. *Pattern Recognit.* (2020) 102:107200. doi: 10.1016/j.patcog.2020.107200
  38. Negahbani F, Sabzi R, Pakniyat Jahromi B, Firouzabadi D, Movahedi F, Kohandel Shirazi M, et al. Pathonet introduced as a deep neural network backend for evaluation of Ki-67 and tumor-infiltrating lymphocytes in breast cancer. *Sci Rep.* (2021) 11:8489. doi: 10.1038/s41598-021-86912-w
  39. Yang M, Nurzynska K, Walts AE, Gertych A. A CNN-based active learning framework to identify mycobacteria in digitized ziehl-neelsen stained human tissues. *Comput Med Imaging Graph.* (2020) 84:101752. doi: 10.1016/j.compmedimag.2020.101752
  40. Stritt M, Stalder AK, Vezzali E. Orbit image analysis: an open-source whole slide image analysis tool. *PLoS Comput Biol.* (2020) 16:e1007313. doi: 10.1371/journal.pcbi.1007313
  41. Bocklitz TW, Salah FS, Vogler N, Heuke S, Chernavskaia O, Schmidt C, et al. Pseudo-HE images derived from CARS/TPEF/SHG multimodal imaging in combination with raman-spectroscopy as a pathological screening tool. *BMC Cancer.* (2016) 16:534. doi: 10.1186/s12885-016-2520-x
  42. Stacke K, Eilertsen G, Unger J, Lundstrom C. Measuring domain shift for deep learning in histopathology. *IEEE J Biomed Health Inform.* (2021) 25:325–36. doi: 10.1109/JBHI.2020.3032060

**Conflict of Interest:** The authors declare that the research was conducted in the absence of any commercial or financial relationships that could be construed as a potential conflict of interest.

**Publisher's Note:** All claims expressed in this article are solely those of the authors and do not necessarily represent those of their affiliated organizations, or those of the publisher, the editors and the reviewers. Any product that may be evaluated in this article, or claim that may be made by its manufacturer, is not guaranteed or endorsed by the publisher.

Copyright © 2022 Jiao, Yuan, Sodimu, Qiang and Ding. This is an open-access article distributed under the terms of the Creative Commons Attribution License (CC BY). The use, distribution or reproduction in other forums is permitted, provided the original author(s) and the copyright owner(s) are credited and that the original publication in this journal is cited, in accordance with accepted academic practice. No use, distribution or reproduction is permitted which does not comply with these terms.